

# Effect of electron-lattice coupling on charge and magnetic order in rare-earth nickelates

Stepan Fomichev <sup>1,2,\*</sup>, Giniyat Khaliullin <sup>3</sup>, and Mona Berciu<sup>1,2</sup>

<sup>1</sup>*Department of Physics and Astronomy, University of British Columbia, Vancouver, British Columbia V6T 1Z1, Canada*

<sup>2</sup>*Stewart Blusson Quantum Matter Institute, University of British Columbia, Vancouver, British Columbia V6T 1Z4, Canada*

<sup>3</sup>*Max Planck Institute for Solid State Research, D-70569 Stuttgart, Germany*

 (Received 13 September 2019; revised manuscript received 3 December 2019; published 6 January 2020)

We investigate the impact of electron-lattice coupling on the stability of various magnetic orders in rare-earth nickelates. We use the Hartree-Fock approximation, at zero temperature, to study an effective two-band model with correlations characterized by a Hubbard  $U$  and a Hund's  $J$ . This is coupled to breathing-mode distortions of the octahedral oxygen cages, described semiclassically with a Holstein term. We analyze the effect of the various parameters on the resulting phase diagram, in particular, on the degree of charge disproportionation and on the magnetic order. We confirm that the coupling to the lattice cooperates with Hund's coupling and thus encourages charge disproportionation. We also find that it favors the four-site periodic magnetic order of type  $\uparrow 0 \downarrow 0$ . Other convergent magnetic phases, such as the collinear  $\uparrow\uparrow\downarrow\downarrow$  and noncollinear  $\uparrow\rightarrow\downarrow\leftarrow$  states, do not couple to the lattice because of their lack of charge disproportionation. Novel phases, e.g., with charge disproportionation but no magnetic order, are found to be stabilized in specific conditions.

DOI: [10.1103/PhysRevB.101.024402](https://doi.org/10.1103/PhysRevB.101.024402)

## I. INTRODUCTION

The rare-earth nickelates  $RNiO_3$ ,  $R$  being any rare-earth element from La to Lu, have generated considerable interest because of their complex phase diagram, where both a metal-insulator transition (MIT) and a magnetic ordering transition can be tuned via pressure, strain, and/or variations in the size of the  $R$  ion (except for  $R = \text{La}$ , which is a metal at all temperatures) [1,2]. Understanding the features of this phase diagram is of significant interest for the advancement of our basic knowledge of strongly correlated systems, but also because of their potential for applications, especially in heterostructures [3] and memory storage [4–6].

The perovskite  $RNiO_3$  consists of Ni ions arranged on a simple cubic lattice with lattice constant  $a$  and connected through the ligand O such that each Ni ion is inside an octahedral cage of oxygen atoms [7]. Standard valence counting suggests the starting configuration to be  $Ni:3d^7$ . Crystal fields split the  $3d$  levels into well-separated  $e_g$  and  $t_{2g}$  manifolds, suggesting a doubly degenerate  $t_{2g}^6 e_g^1$  configuration that should be unstable to Jahn-Teller distortions [8]. Such distortions are not observed experimentally [9], so the  $e_g$  degeneracy must be resolved in some other way. Many scenarios have been proposed, including, most notably, (i) charge disproportionation (CD), originally proposed as an alternative to the Jahn-Teller distortion [1,10,11], and (ii) a negative charge-transfer (NCT) energy [12–17].

The CD scenario posits that below the MIT there are two inequivalent Ni sites with different charge,  $3d^7 3d^7 \rightarrow 3d^{7-\delta} 3d^{7+\delta}$ ; this is then thought to drive the experimentally observed distortion [18] of the O octahedra into small/large ones around the two inequivalent Ni sites. As typical for

strongly correlated insulators, magnetic order also develops at or below the MIT phase line.

In contrast, the NCT scenario has all the Ni in the  $3d^8$  ( $S = 1$ ) configuration, with each releasing a ligand hole into the O band. The resulting 1/6 filled (with holes) O band is metallic at high temperatures. In this view, the MIT is primarily due to electron-phonon coupling, which distorts the O octahedra into small and large ones ( $pp$  and  $pd$  hopping are enhanced on the shorter bonds), resulting in pairs of ligand holes localized on the small octahedra and locked into a singlet with their central Ni. The spins of the Ni ions located in the large cages, on the other hand, order magnetically at or below the MIT temperature.

The electron-phonon coupling is obviously important for the MIT transition in both scenarios (even if in rather different ways), but its impact on the magnetic order is not well understood. Neutron-scattering experiments on powders [19,20] indicate a magnetic ordering wave vector  $\mathbf{Q}_m = \frac{\pi}{2a}(1, 1, 1)$  in pseudocubic notation [equivalently,  $\frac{\pi}{2a}(1, 0, 1)$  in orthorhombic notation], which is half of the value associated with the lattice distortion ordering (and charge modulation, in the CD scenario) of  $\mathbf{Q}_c = \frac{\pi}{a}(1, 1, 1)$ . The orientations and magnitudes of the local magnetic moments in the four-site (counting Ni only) magnetic unit cell are still under debate. Three leading contenders are the fully disproportionated antiferromagnetic state  $\uparrow 0 \downarrow 0$  [21] and two partially disproportionated orders: the collinear order  $\uparrow\uparrow\downarrow\downarrow$  [22] and the noncollinear order  $\uparrow\rightarrow\downarrow\leftarrow$  [9,23]. (Throughout this work we use fat arrows to indicate larger spin magnitudes.)

While the preferred magnetic order is likely to be primarily decided by the electron-electron interactions, as is generally the case in strongly correlated systems, it is possible that the strong coupling to the lattice also plays an important role by favoring or hindering some of these possible candidates. We study this possibility here using an effective

\*fomichev@physics.ubc.ca

two-orbital Hamiltonian that, within the appropriate framework (discussed below), can be used to model both the CD and the NCT scenarios. Our work builds on that of Lee *et al.* [22], who studied magnetic orders possible in similar multiorbital models. The main novelty is that our model also includes coupling to the lattice at the semiclassical level.

We verify that the electron-lattice coupling favors insulating charge order, consistent with earlier work. While a number of four-site magnetic orders, including  $\uparrow 0 \downarrow 0$ ,  $\uparrow\uparrow\downarrow\downarrow$ , and  $\uparrow\rightarrow\downarrow\leftarrow$ , are self-consistent within our model, we find that  $\uparrow 0 \downarrow 0$  is the only one that has nonzero charge modulation  $\delta \neq 0$ : as such it is strongly favored by the electron-lattice coupling. The other magnetic orders  $\uparrow\uparrow\downarrow\downarrow$  and  $\uparrow\rightarrow\downarrow\leftarrow$  are only self-consistent when  $\delta = 0$  and as a result do not couple to the lattice in our model. As the strength of the electron-lattice coupling increases, we also find a novel stable phase where charge modulation occurs without any magnetic order.

The paper is organized as follows: In Sec. II, we describe our effective model Hamiltonian. Section III reviews the Hartree-Fock calculation used to study it, as well as its numerical implementation. In Sec. IV we present and discuss our results. Finally, Sec. V contains our conclusions.

## II. THE MODEL

We consider a simple cubic lattice, with lattice constant  $a = 1$ . At each site  $i$ , two  $e_g$  “effective” orbitals  $|z\rangle \equiv |3z^2 - r^2\rangle$  and  $|\bar{z}\rangle \equiv |x^2 - y^2\rangle$  are active, and  $d_{iz\sigma}^\dagger, d_{i\bar{z}\sigma}^\dagger$  are the electronic creation operators associated with them. The physical connection to the actual material of these and the other “effective” degrees of freedom that we introduce below is discussed after the Hamiltonian is fully defined. The Hamiltonian we study is defined as

$$\hat{H} = \hat{T} + \hat{H}_{e-e} + H_{lat} + \hat{H}_{e-lat}. \quad (1)$$

The kinetic energy  $\hat{T} = \hat{T}_1 + \hat{T}_2 + \hat{T}_4$  includes up to fourth-nearest-neighbor hopping. The hopping term  $\hat{T}_1$  includes hopping between nearest-neighbor  $|z\rangle$  orbitals along the  $z$  axis and between  $|x\rangle \equiv |3x^2 - r^2\rangle$  and  $|y\rangle \equiv |3y^2 - r^2\rangle$  orbitals along the  $x$  and  $y$  axes, respectively. There is no nearest-neighbor hopping in the  $z$  direction between  $|\bar{z}\rangle$  orbitals, etc., because these orbitals are orthogonal to their corresponding ligand O. As a result,

$$\hat{T}_1 = -t_1 \sum_{i\sigma} \sum_{\eta=x,y,z} (d_{i+\eta,\sigma}^\dagger d_{i,\sigma} + \text{H.c.}). \quad (2)$$

This can be easily expressed in terms of the  $d_{iz\sigma}^\dagger, d_{i\bar{z}\sigma}^\dagger$  operators using the identities

$$\begin{aligned} d_{ix\sigma}^\dagger &= -\frac{1}{2}d_{iz\sigma}^\dagger + \frac{\sqrt{3}}{2}d_{i\bar{z}\sigma}^\dagger, \\ d_{iy\sigma}^\dagger &= -\frac{1}{2}d_{i\bar{z}\sigma}^\dagger - \frac{\sqrt{3}}{2}d_{iz\sigma}^\dagger. \end{aligned} \quad (3)$$

Similarly, we define second-nearest-neighbor and fourth-nearest-neighbor hopping terms  $\hat{T}_2$  and  $\hat{T}_4$ , respectively, keeping all such terms that have finite hopping amplitudes. Collecting all terms and after a Fourier transform to the  $\mathbf{k}$ -space

basis, defined as

$$d_{\mathbf{k}a\sigma}^\dagger = \frac{1}{\sqrt{N}} \sum_i e^{i\mathbf{k}\mathbf{R}_i} d_{ia\sigma}^\dagger, \quad (4)$$

where  $a = z, \bar{z}$ ,  $N \rightarrow \infty$  is the number of sites in the system with periodic boundary conditions, and  $\mathbf{k}$  is defined inside the full Brillouin zone  $-\pi < k_\eta \leq \pi$ ,  $\eta = x, y, z$ , the hopping Hamiltonian is brought to the standard form

$$\hat{T} = \sum_{\mathbf{k}ab\sigma} t_{ab}(\mathbf{k}) d_{\mathbf{k}a\sigma}^\dagger d_{\mathbf{k}b\sigma}. \quad (5)$$

The coefficients  $t_{ab}(\mathbf{k})$  are listed in the Appendix.

The on-site electron-electron interactions are described by the Kanamori Hamiltonian [24–26]:

$$\begin{aligned} \hat{H}_{e-e} &= U \sum_{ia} \hat{n}_{ia\uparrow} \hat{n}_{ia\downarrow} + U' \sum_{i\sigma} \hat{n}_{iz\sigma} \hat{n}_{i\bar{z}\sigma} \\ &+ (U' - J) \sum_{i\sigma} \hat{n}_{iz\sigma} \hat{n}_{i\bar{z}\sigma} - J \sum_{i\sigma} d_{iz\sigma}^\dagger d_{i\bar{z}\sigma} d_{i\bar{z}\sigma}^\dagger d_{iz\sigma} \\ &+ J \sum_{ia} d_{ia\uparrow}^\dagger d_{i\bar{a}\uparrow}^\dagger d_{ia\downarrow}^\dagger d_{i\bar{a}\downarrow}, \end{aligned} \quad (6)$$

with the spherically symmetric choice  $U' = U - 2J$  [27]. Here,  $\hat{n}_{ia\sigma} = d_{ia\sigma}^\dagger d_{ia\sigma}$  counts the electrons with spin  $\sigma$  in the  $a = z, \bar{z}$  orbital at site  $i$ , and  $\hat{n}_i = \sum_{a\sigma} \hat{n}_{ia\sigma}$ . We use this full form of  $\hat{H}_{e-e}$  as opposed to the simpler one used in Lee *et al.* [22] because it leads only to minor complications in the mean-field treatment and has a formal derivation based on allowed Coulomb intraionic interactions [23–25]. This change explains the quantitative differences between our results—in the absence of coupling to the lattice—and those of Lee *et al.*

Next,  $H_{lat}$  describes, at the semiclassical level, the breathing-mode distortion resulting in contracted and expanded octahedra:

$$H_{lat} = \sum_i \left( \frac{k}{2} (\delta U_i)^2 + \frac{A}{4} (\delta U_i)^4 \right),$$

where  $\delta U_i$  is the (isotropic) change in the Ni-O bond length of the octahedral cage surrounding site  $i$ , and we include quartic anharmonicity to ensure reasonable values for these distortions.

The octahedral distortions affect the on-site electron energies and hence the electron-lattice interaction term:

$$\hat{H}_{e-lat} = -g \sum_i \delta U_i (\hat{n}_i - 1).$$

It is convenient to use dimensionless variables  $u_i = (\delta U_i)k/g$ , in terms of which we rewrite

$$H_{lat} + \hat{H}_{e-lat} = 2\epsilon_b \sum_i \left( \frac{1}{2}u_i^2 + \frac{\alpha}{4}u_i^4 \right) - 2\epsilon_b \sum_i u_i (\hat{n}_i - 1), \quad (7)$$

where  $\epsilon_b = g^2/2k$  is the energy gain from of the breathing-mode distortion for  $u_i = 1, \alpha = 0$ , and  $\alpha \propto A$  is the dimensionless parameter characterizing the anharmonicity. To summarize, there are seven parameters characterizing this Hamiltonian: the three hoppings  $t_1, t_2, t_4$ , the on-site Coulomb repulsion  $U$  and Hund’s exchange  $J$ , the electron-lattice

coupling strength  $\epsilon_b$ , and the dimensionless anharmonicity parameter  $\alpha$ .

Before concluding this section, we comment on how this Hamiltonian describes the two scenarios discussed above. Within the CD scenario, only the Ni  $e_g$  orbitals are relevant as valence orbitals, so they should be directly identified with the  $e_g$  orbitals of this model. In this view, the O are electronically inert and serve only to modulate the on-site energy at the Ni sites when the cages are distorted. Even though the octahedra are known to tilt and rotate, the Ni-O distances stay equal inside each cage, so it is reasonable to use a single distortion  $u_i$  to characterize each octahedron. Note that while our model does not explicitly impose constraints between distortions on neighboring cages, the mean-field solution will turn out to satisfy them, as discussed below.

The relevance to the NCT scenario is less obvious. Here, a full description of the electronic degrees of freedom include not only the Ni  $e_g$  orbitals but also the ligand O  $2p$  ones, as discussed in Ref. [17]. Of course, in principle one could do a mean-field treatment on the Hamiltonian used there to discuss the MIT in order to find what magnetic order it favors and how (or if) it is affected by the fact that the O displacements modulate the hopping amplitudes. The difficulty is that the magnetic unit cell contains 4 Ni together with their 12 O, i.e., 20 distinct orbitals. Needless to say, when combined with the multitude of possible mean-field parameters in such a large basis, the problem becomes rather unwieldy.

On the other hand, when considering a single Ni plus its O octahedron, one finds that the relevant eigenstates on the O sites are linear combinations with the same  $e_g$  symmetries as the atomic Ni orbitals. This is because in order for an electron from the O band to move in the  $e_g$  Ni manifold (and thus leave behind a ligand hole), it has to come from an O state that will hybridize (via  $t_{pd}$  hopping) with the Ni orbital, and that occurs only if they have the same point symmetry. This is what allows us to identify the two  $e_g$  “effective” orbitals as being these O-based linear combinations with the correct  $e_g$  symmetry, surrounding various Ni sites and into which the ligand hole can go [28]. The complication here is that such orbitals centered about nearest-neighbor Ni ions are not orthogonal, so the true “effective” orbitals must correct for that and are therefore somewhat more extended and more complicated than simple linear combinations of O orbitals on each octahedral cage. As a result, all hoppings and electronic parameters are strongly renormalized from their atomic values. We do not attempt to estimate their realistic values; instead, we will treat them as free parameters. This allows us to investigate what kind of magnetic orders arise in different regions of this large parameter space and thus cover simultaneously both the CD and the NCT scenarios (their parameters are likely to be quite different).

In a broader view, the CD and NCT scenarios are limiting cases in a continuum of possibilities. The  $t_{pd}$  hopping always leads to some hybridization between the Ni  $e_g$  states and O-based states of the same symmetry. If the O bands are well below the Ni levels (for a large, positive charge-transfer energy compared to  $|t_{pd}|$ ), then these hybridized states are predominantly located on the Ni; this is the CD scenario. On the other hand, if the charge-transfer energy is very negative, then the hybridized states will live primarily on the O; this corresponds

to the NCT scenario. The reality is likely to be somewhere in between, where the probability to be on the Ni is neither 1 nor 0. Our effective model describes this entire continuum of possibilities for appropriate choices of the parameters.

### III. HARTREE-FOCK CALCULATION

We study the Hamiltonian of Eq. (1) within the Hartree-Fock approximation. As usual, this implies finding the global minimum of the average energy

$$E(\{u\}) = \langle \Psi_e | \hat{H}(\{u\}) | \Psi_e \rangle, \quad (8)$$

where the Slater determinant  $|\Psi_e\rangle$  describes the electronic part, and the set  $\{u\} = (u_1, u_2, \dots)$  characterizes the semiclassical distortions of the lattice.

#### A. Lattice contributions

First, we minimize the energy with respect to the lattice distortions  $u_i$ . This can be done easily using the Hellmann-Feynman theorem [29,30]:

$$\frac{d}{du_j} E(\{u\}) = \langle \Psi_e | \frac{\partial \hat{H}(\{u\})}{\partial u_j} | \Psi_e \rangle. \quad (9)$$

Note that Eq. (9) holds despite the fact that  $|\Psi_e\rangle$  is not an eigenstate of  $\hat{H}(\{u\})$  (as assumed in the usual proof [31]). This is because a stronger proof is available, one that shows the theorem to hold for any sufficiently optimized variational state, not just for exact eigenstates [32] (in our case, we also confirmed this numerically). An optimal variational state  $|\Psi_e\rangle$  satisfies the stationarity condition:  $\frac{\delta E}{\delta \Psi_e(u)} = 0$  (this is a shorthand notation replacing all the derivatives with respect to all the one-particle orbitals defining  $|\Psi_e\rangle$ ). This condition justifies why the second term vanishes in the identity  $\frac{d}{du_j} E(\{u\}) = \frac{\partial E(\{u\})}{\partial u_j} + \frac{\delta E(\{u\})}{\delta \Psi_e(u)} \frac{\partial \Psi_e(u)}{\partial u_j}$ , which then leads to Eq. (9).

Thus, for our Hamiltonian we obtain the minimization condition at each site  $j$

$$u_j + \alpha u_j^3 = \langle \hat{n}_j \rangle - 1, \quad (10)$$

where from now on we use the shorthand notation  $\langle \hat{O} \rangle = \langle \Psi_e | \hat{O} | \Psi_e \rangle$  for any electronic operator.

To make further progress, we use the experimentally well-established fact [18] that the octahedra alternate between expanded and collapsed ones, so that  $u_j = u e^{i\mathbf{Q}_c \cdot \mathbf{R}_j}$ , where  $\mathbf{Q}_c = \pi(1, 1, 1)$  (here and throughout the rest of the text the lattice constant has been set to 1). This immediately implies the appearance of a charge modulation  $\langle \hat{n}_j \rangle = 1 + \delta e^{i\mathbf{Q}_c \cdot \mathbf{R}_j}$ , where the amplitude of the lattice distortion  $u$  is directly linked to the amplitude of the charge modulation  $\delta$  by

$$u + \alpha u^3 = \delta. \quad (11)$$

This equation shows that in our model, the existence of a charge modulation  $\delta \neq 0$  forces the appearance of a lattice distortion  $u \neq 0$ , and vice versa. This depressed [33] cubic equation admits the exact solution using Cardano's formula

(see Appendix B for details):

$$u = \delta \frac{3}{2\beta^{\frac{1}{3}}} \left[ \left( \sqrt{1 + \frac{1}{\beta}} + 1 \right)^{\frac{1}{3}} - \left( \sqrt{1 + \frac{1}{\beta}} - 1 \right)^{\frac{1}{3}} \right], \quad (12)$$

with  $\beta = \frac{27}{4}\alpha\delta^2$ .

It is useful to consider this expression in some limiting cases: in the case of vanishing anharmonicity,  $\alpha \rightarrow 0$ , already from Eq. (11) we see that  $u = \delta$ . For a fixed value of  $\delta$ , increased anharmonicity  $\alpha$  will lead to a decrease of  $u$ . Indeed, in the case of infinite anharmonicity,  $\beta \rightarrow \infty$  and we find

$$u \approx \delta \frac{3}{2\beta^{\frac{1}{3}}} [2^{1/3}] \rightarrow 0. \quad (13)$$

The exact solution listed in Eq. (12) is very convenient because it allows us to substitute for any  $u$  dependence in the Hartree-Fock equations (discussed next) and have them depend only on the electronic mean fields.

## B. Electronic contributions

We follow the usual steps, briefly summarized here for completeness, to derive the Hartree-Fock (HF) equations. Any Slater determinant has the general form

$$|\Psi_e\rangle = \prod_p a_p^\dagger |0\rangle,$$

where the appropriate number of electrons (here equal to the number of sites) is created. The new and the old states are related by a unitary transformation

$$d_{i\alpha\sigma}^\dagger = \sum_n \phi_n^*(i\alpha\sigma) a_n^\dagger.$$

The goal is to determine the optimal  $\phi_n(i\alpha\sigma)$  which minimize the total energy  $E(\{u\}) = \langle \hat{H}(\{u\}) \rangle$ . The evaluation of this expectation value, and its minimization with respect to all properly normalized  $\phi_n(i\alpha\sigma)$  proceeds in the usual way. As always, the resulting HF equations depend on various mean-field expectation values  $\langle d_{i\alpha\sigma}^\dagger d_{i\beta\sigma'} \rangle$  (because all interactions are local, terms with  $i \neq j$  do not appear).

We constrain these mean fields to have the most general forms consistent with the four-site unit cell found experimentally in the magnetically ordered state. Specifically, we set

$$\langle d_{i\alpha\sigma}^\dagger d_{i\alpha\sigma} \rangle = \frac{1}{4} [1 + \delta e^{i\mathbf{Q}_c \cdot \mathbf{R}_i}] + \frac{\sigma}{2} [S_{\text{FM}} + S_{\text{AFM}} e^{i\mathbf{Q}_c \cdot \mathbf{R}_i} + S_{1z} \cos(\mathbf{Q}_m \cdot \mathbf{R}_i) + S_{2z} \sin(\mathbf{Q}_m \cdot \mathbf{R}_i)], \quad (14)$$

$$\langle d_{i\alpha\sigma}^\dagger d_{i\bar{\alpha}\bar{\sigma}} \rangle = \frac{1}{2} [S_{1x} \cos(\mathbf{Q}_m \cdot \mathbf{R}_i) + S_{2x} \sin(\mathbf{Q}_m \cdot \mathbf{R}_i)], \quad (15)$$

$$\langle d_{i\alpha\sigma}^\dagger d_{i\bar{\alpha}\sigma} \rangle = O_1 + O_2 e^{i\mathbf{Q}_c \cdot \mathbf{R}_i} + \sigma [Z_1 + Z_2 e^{i\mathbf{Q}_c \cdot \mathbf{R}_i} + Z_3 \cos(\mathbf{Q}_m \cdot \mathbf{R}_i) + Z_4 \sin(\mathbf{Q}_m \cdot \mathbf{R}_i)], \quad (16)$$

$$\langle d_{i\alpha\sigma}^\dagger d_{i\bar{\alpha}\bar{\sigma}} \rangle = X_1 \cos(\mathbf{Q}_m \cdot \mathbf{R}_i) + X_2 \sin(\mathbf{Q}_m \cdot \mathbf{R}_i). \quad (17)$$

Equation (14) is consistent with the condition that  $\langle \hat{n}_i \rangle = \sum_{\alpha,\sigma} \langle d_{i\alpha\sigma}^\dagger d_{i\alpha\sigma} \rangle = 1 + \delta e^{i\mathbf{Q}_c \cdot \mathbf{R}_i}$ . The other terms in Eq. (14) allow for various possible magnetic orders with a nonvanishing  $z$ -axis spin expectation value:

$$\langle \hat{S}_{i,z} \rangle = \frac{1}{2} \sum_{\alpha,\sigma} \sigma \langle d_{i\alpha\sigma}^\dagger d_{i\alpha\sigma} \rangle = S_{\text{FM}} + S_{\text{AFM}} e^{i\mathbf{Q}_c \cdot \mathbf{R}_i} + S_{1z} \cos(\mathbf{Q}_m \cdot \mathbf{R}_i) + S_{2z} \sin(\mathbf{Q}_m \cdot \mathbf{R}_i). \quad (18)$$

If only  $S_{\text{FM}} \neq 0$ , the order is ferromagnetic (FM), or  $\uparrow\uparrow\uparrow\uparrow$  (for simplicity, we show the order inside only one four-site unit cell); if only  $S_{\text{AFM}} \neq 0$ , the order is antiferromagnetic (AFM)  $\uparrow\downarrow\uparrow\downarrow$ ; finally, having  $S_{1z} \neq 0$  or  $S_{2z} \neq 0$  further breaks translational symmetry, resulting in states with order like  $\uparrow 0 \downarrow 0$  and  $0 \uparrow 0 \downarrow$ , respectively. Combinations of two or more finite expectation values lead to yet more possibilities, for example, having both  $S_{\text{FM}} \neq 0$ ,  $S_{\text{AFM}} \neq 0$  implies a ferrimagnetic order  $\uparrow\downarrow\uparrow\downarrow$  or  $\uparrow\uparrow\uparrow\uparrow$ , depending on the relative magnitude of the parameters, etc. Note that this choice of mean-field parametrization assumes *a priori* equal orbital occupancy  $\langle n_{iz} \rangle = \langle n_{i\bar{z}} \rangle$ , ruling out the possibility of Jahn-Teller distortions. This is justified by the lack of experimental observation of Jahn-Teller distortions in these materials.

Equation (15) allows for noncollinear magnetic orders because a finite  $S_{1x}$  and/or  $S_{2x}$  imply nonvanishing  $\langle \hat{S}_{i,x} \rangle$ . In particular, a solution with finite  $S_{1z} = S_{2x}$  and all other values set to zero is the order  $\uparrow \rightarrow \downarrow \leftarrow$ , which is one of the possible candidates. To conclude, Eqs. (14) and (15) allow the realization of any magnetic order with a four-site unit cell consistent with the ordering vector  $\mathbf{Q}_m = \mathbf{Q}_c/2$ .

Similarly, Eqs. (16) and (17) allow for various orbital and magnetic + orbital orders, respectively. To the best of our knowledge, there is no experimental signature of any orbital ordering in the rare-earth nickelates [9], and numerical calculations suggest that orbital order states are expected to be relatively high energy [34]. Previous work found orbitally ordered ground states for  $U'/W \approx (U - 2J)/6 > 2$  [35]. Here,  $W \sim 6$  is the bandwidth of the noninteracting system for  $t_1 = 1$  and  $t_2, t_4 < 0.3$ . For a realistic  $J/t_1 \sim 1-2$ , this implies  $U/t_1 > 14-16$ , which is enough to stabilize a conventional spin and orbital ordered Mott phase with no charge disproportionation. Our model is consistent with this, in the sense that the lowest energy self-consistent states for experimentally reasonable values of the charge modulation  $\delta$  always have vanishing  $O, X, Z$  values. However, we have also found regions of parameter space where orbital ordered states appear to have the lowest energy, as discussed below. For

convenience, in the following we will still set  $\langle d_{i\alpha\sigma}^\dagger d_{i\alpha\sigma} \rangle = 0$  so as to keep the equations shorter, with the full form available in the Appendix. We emphasize that in the regions of parameter space relevant to us, i.e., the neighborhood of the region where  $\delta \sim 0.3\text{--}0.4$ , we have tested explicitly that the ground states do not exhibit orbital order (in agreement with experimental observations) by running self-consistency loops where these mean fields  $O, X, Z$  had finite initial values.

$$\begin{aligned}
H_{\text{eff}} = & \sum_{\mathbf{k}ab\sigma} t_{ab}(\mathbf{k}) c_{\mathbf{k}a\sigma}^\dagger c_{\mathbf{k}b\sigma} + \sum_{\mathbf{k}a\sigma} \left[ \frac{3U - 5J}{4} - \frac{\sigma}{2}(U + J)S_{\text{FM}} \right] c_{\mathbf{k}a\sigma}^\dagger c_{\mathbf{k}a\sigma} \\
& + \sum_{\mathbf{k}a\sigma} \left[ \frac{3U - 5J}{4} \delta - 2\epsilon_b u - \frac{\sigma}{2}(U + J)S_{\text{AFM}} \right] c_{\mathbf{k}+\mathbf{Q}_c, a\sigma}^\dagger c_{\mathbf{k}a\sigma} \\
& - \frac{\sigma}{4}(U + J) \sum_{\mathbf{k}a\sigma} [(S_{1z} - iS_{2z})c_{\mathbf{k}+\mathbf{Q}_m, a\sigma}^\dagger c_{\mathbf{k}a\sigma} + (S_{1z} + iS_{2z})c_{\mathbf{k}-\mathbf{Q}_m, a\sigma}^\dagger c_{\mathbf{k}a\sigma}] \\
& - \frac{U + J}{4} \sum_{\mathbf{k}a\sigma} [(S_{1x} - iS_{2x})c_{\mathbf{k}+\mathbf{Q}_m, a\sigma}^\dagger c_{\mathbf{k}a\sigma} + (S_{1x} + iS_{2x})c_{\mathbf{k}-\mathbf{Q}_m, a\sigma}^\dagger c_{\mathbf{k}a\sigma}]. \tag{19}
\end{aligned}$$

This Hamiltonian has four more similar lines of terms involving various  $O, Z, X$  mean fields which we do not write here explicitly, as discussed above. We remind the reader that the lattice parameter  $u$  appearing in the second line is given by Eq. (12).

After Fourier transforming,  $H_{\text{eff}} = \sum_{\mathbf{k}} \psi_{\mathbf{k}}^\dagger h(\mathbf{k}) \psi_{\mathbf{k}}$ , where  $\psi_{\mathbf{k}}^\dagger = (\psi_{\mathbf{k}z\uparrow}^\dagger, \psi_{\mathbf{k}z\downarrow}^\dagger, \psi_{\mathbf{k}z\uparrow}^\dagger, \psi_{\mathbf{k}z\downarrow}^\dagger)$  and  $\psi_{\mathbf{k}a\sigma}^\dagger = (c_{\mathbf{k}a\sigma}^\dagger, c_{\mathbf{k}+\mathbf{Q}_m, a\sigma}^\dagger, c_{\mathbf{k}+\mathbf{Q}_c, a\sigma}^\dagger, c_{\mathbf{k}-\mathbf{Q}_m, a\sigma}^\dagger)$ . The  $16 \times 16$  matrix  $h(\mathbf{k})$  can be directly read from Eq. (19) and is trivial to diagonalize numerically.

The self-consistent HF ground state is then straightforward to find, at least in principle. We start with an initial guess for the mean-field parameters  $\mathbf{w}^{(0)} = (\delta^{(0)}, S_{\text{FM}}^{(0)}, S_{\text{AFM}}^{(0)}, \dots)$ . These can be chosen either so as to test if a certain state, e.g.  $\uparrow \rightarrow \downarrow \leftarrow$ , is self-consistent or by choosing random values for all these fields. We have always checked all the ‘‘simple’’ magnetic orders to see if they are self-consistent and if yes, what is their corresponding energy. However, in all cases we have also run a multitude of searches starting with random initial conditions to make sure we are not missing a better candidate.

Once the mean-field parameters are chosen, the Hamiltonian (19) is diagonalized at all allowed  $\mathbf{k}$  points in the Brillouin zone, and its ground state at quarter filling is identified. Using it, we compute the new mean-field parameters  $\mathbf{v}^{(0)} = (\delta^{(0)}, S_{\text{FM}}^{(0)}, S_{\text{AFM}}^{(0)}, \dots)$  based on Eqs. (14)–(17). For example,  $\delta^{(0)} = \frac{1}{N} \sum_{i\alpha\sigma} e^{i\mathbf{Q} \cdot \mathbf{R}_i} \langle \hat{n}_{i\alpha\sigma} \rangle = \frac{1}{N} \sum_{\mathbf{k}a\sigma} \langle c_{\mathbf{k}+\phi_c, a\sigma}^\dagger c_{\mathbf{k}a\sigma} \rangle$ , etc. We then compute the residual  $\epsilon^{(0)} = |\mathbf{v}^{(0)} - \mathbf{w}^{(0)}|^2$ . If this is below the desired accuracy, then convergence has been reached. If not, we set new values for the mean-field parameters:  $\mathbf{w}^{(1)} = \mathbf{v}^{(0)}$  (a simplification, in reality we use a better choice, discussed below), and iterate until either the desired accuracy is reached or the maximum iteration count is surpassed and this search is abandoned.

Once self-consistency is reached, i.e.,  $\mathbf{w} \approx \mathbf{v}$ , the total energy associated with the set  $\mathbf{w}$  of mean-field parameters is

The resulting self-consistent solutions either converged to vanishing values for these orbital mean fields or had much higher total energy than self-consistent states without orbital order, in accord with earlier findings [34].

The corresponding HF equations are identical to those arising from a noninteracting Hamiltonian  $\hat{H}_{\text{eff}}$  (which can be thought of as being the properly factorized counterpart of the original  $\hat{H}$ ):

given by

$$\frac{E}{N} = \frac{1}{N} \sum_p E_p - \frac{1}{N} \langle \hat{H}_{e-e} \rangle + 2\epsilon_b \left( \frac{u^2}{2} + \frac{au^4}{4} \right). \tag{20}$$

Here  $E_p$  are the eigenenergies of the occupied states, and

$$\begin{aligned}
\langle \hat{H}_{e-e} \rangle = & \frac{3U - 5J}{8} (1 + \delta^2) - \frac{U + J}{2} \\
& \times \left( S_{\text{FM}}^2 + S_{\text{AFM}}^2 + \frac{S_{1x}^2 + S_{1z}^2 + S_{2x}^2 + S_{2z}^2}{2} \right) \tag{21}
\end{aligned}$$

(again, terms proportional to the  $O, Z, X$  fields are omitted here and are instead given in the Appendix).

After multiple searches for various initial conditions, the set  $\mathbf{w} \approx \mathbf{v}$ , corresponding to the lowest total energy  $E$ , is declared as the HF ground state, and its magnetic (and charge, orbital, lattice...) order is read off from its mean-field parameters.

While all this seems straightforward, in reality the problem is complicated by the large number of mean-field parameters whose convergence is sought: 15 when the  $O, Z, X$  fields are included explicitly, and 7 otherwise. Searching for a local minimum in this many-dimensional space is nontrivial, and for too simplistic update rules such as  $\mathbf{w}^{(n+1)} = \mathbf{v}^{(n)}$ , it can take extremely many iteration steps before self-consistency is reached, if it is reached at all.

Because of this, we briefly mention here a few strategies that we found very useful:

(a) A much better update is an interpolation of the type

$$\mathbf{w}^{(n+1)} = \alpha \mathbf{v}^{(n)} + (1 - \alpha) \mathbf{w}^{(n)}. \tag{22}$$

The literature on nonlinear iterative equation solution techniques suggests that the choice of the mixing parameter  $\alpha$  is typically problem specific [36]. We find the smoothest and most reliable convergence over most of the parameter space of interest occurs for  $\alpha = 0.3$ . This type of update can avoid

the iteration of being stuck in a loop or helplessly hopping on either side of a “flat minimum.”

(b) However, we found that this approach works best in conjunction with Pulay mixing, or direct inversion in the iterative subspace (DIIS). The idea behind DIIS, originally developed for high-parameter Hartree-Fock quantum chemistry calculations by Pulay [37], is as follows: Suppose that a sequence of solutions  $\mathbf{v}^{(n+1)}, \mathbf{v}^{(n+2)}, \dots, \mathbf{v}^{(n+N)}$  to the nonlinear system has been generated from some initial solution step  $n$ . Together, they span a linear subspace  $W_{N,n} = \text{span}\{\mathbf{v}^{(n+1)}, \mathbf{v}^{(n+2)}, \dots, \mathbf{v}^{(n+N)}\}$  within the higher-dimensional (possibly nonlinear) parameter manifold  $W$ . It is then possible to pick the “best possible” vector  $\mathbf{w}^{(N)}$  within this linear subspace by minimizing the error  $\epsilon = \|\sum_i^N \mathbf{v}^{(i)} - \mathbf{w}^{(i)}\|^2$ , which amounts to solving an  $N + 1 \times N + 1$  system of linear equations (hence the “inversion of the iterative subspace”—for more details, see Ref. [37]).

The DIIS can quickly maximize the potential of the vectors within the subspace  $W_{N,n}$ , but if the true solution is outside the subspace by more than the allowed residual  $\epsilon_0$ , then no matter how many times the Pulay mixing is carried out, it will not result in improved convergence. The solution [36] is to intersperse Pulay mixing with regular updates of the form (22) with a given periodicity  $k$  (typically  $k = 3$ ). The algorithm thus alternates between expanding its iterative subspace and finding the lowest residual vector within it, resulting in optimal convergence for most parameter values. Our experience is that it can even arrest divergences from round-off error accumulation. Often even small errors (say, in mean fields that should be zero for a particular type of converged state) can lead to rapid divergence of the HF iterative trajectory away from a self-consistent point. Yet DIIS appears to nullify that tendency, restoring the mean-field magnitudes back to zero and guiding the trajectory towards the self-consistent point.

(c) Parallelization: While the iterative loop is not easy to parallelize efficiently, there are higher-level parallelization opportunities: (i) multiple initial guesses can be iterated in parallel for a given set of parameter values  $U, J, \epsilon_b, t_1, \dots$ , and (ii) ground states can be found at multiple parameter values, in parallel. We opted for option (ii) due to ease of implementation and data management, together with linear speed-up of the calculation (because ground states corresponding to different parameter values are independent from each other, there is no overhead to the parallelization).

(d) Boot-strapping: While calculations at neighboring points in the parameter space are independent from each other, we expect small changes in the values of the various parameters  $U, J, \epsilon_b, t_1, \dots$  to normally lead to small changes in the nature of the ground state  $\mathbf{w}$ . As such, an already converged solution from a neighboring point can result in fast convergence to a similar kind of converged solution at the current point. Where available, we included this option in the set of initial mean-field guesses.

Finally, we found that there are two key parameters that need to be tested for convergence: the cutoff iteration count  $n_{\text{max-iter}}$  and the number of points sampled in the Brillouin zone  $n_{\text{num-k-pts}} = N^3$ . The sampling of the momentum space slows down the calculation time  $\sim \mathcal{O}(N^3)$ , so choosing too

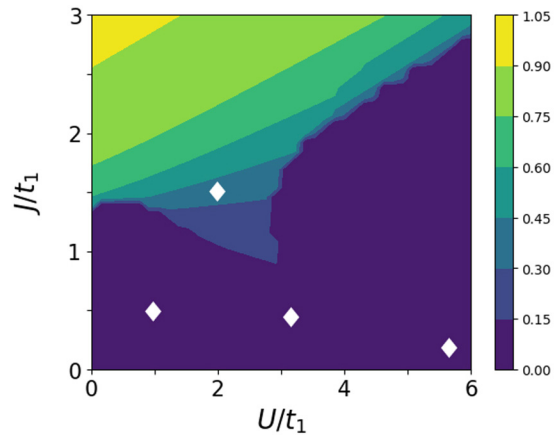


FIG. 1. Charge modulation  $\delta$  (see color scale) in the HF ground state in the  $U$ - $J$  plane. Other parameters are  $t_1 = 1, t_2 = 0.15, t_4 = 0, \epsilon_b = 0$ . Resolution is  $40 \times 40$ . The white diamonds indicate the locations at which the densities of states are plotted in Fig. 2.

large an  $N$  is costly while too low a value introduced finite-size effects. Similarly, the cutoff iteration count needs to be large enough to allow convergence for the interesting solutions but not so large as to waste computation time on “dead-end” iterative trajectories that never converge. We found  $N = 25$  and  $n_{\text{max-iter}} = 500$  to be optimal for our purposes, taming the error in mean fields to below  $\epsilon_0 = 10^{-4}$  and in ground-state energies to less than  $10^{-3}$ .

In total, to obtain a typical phase diagram, we carry out anywhere from 400 to 1600 calculations (depending on the desired resolution), each of which starts from a pool of 20–30 initial guesses and proceeds through anywhere from 5 to 500 iterative steps (where each iterative step involves the diagonalization of roughly 15 000  $16 \times 16$  sub-blocks of the Hartree-Fock matrix, as well as the calculation of the density matrix and the order parameters  $\mathbf{w}$ ).

#### IV. RESULTS

The results shown here focus on areas of the phase diagram with essentially no orbital order. As mentioned, our searches for converged self-consistent states with nontrivial orbital order never produced a viable candidate for an HF ground state in the region of the parameter space with finite charge modulation  $\delta \sim 0.3$ – $0.4$ . However, we did find that sometimes orbitally ordered states were indeed the ground-state configuration in other regions of the phase diagram, namely, towards the large- $U$  Mott limit. Most notably, the antiferromagnetic ferro-orbital order,  $\uparrow\downarrow\uparrow\downarrow + XxXx$  (marked “afm-ferroorb” in the phase diagrams below), and other orbitally ordered possibilities (marked miscellaneous, or “misc”). Given that such orders are found outside the experimentally relevant parameter regime, from now on we focus only on the HF parameters  $\delta, S_{\text{FM}}, S_{\text{AFM}}, S_{1z/x}, S_{2z/x}$  and leave the investigation of the regions with stable orbital order to future work. The lattice distortion  $u$  is related to  $\delta$  through Eq. (12).

To get a basic idea of the dependence of the charge modulation  $\delta$  on the electronic interaction strengths  $U$  and  $J$ , we start by showing in Fig. 1 a contour plot of the charge modulation

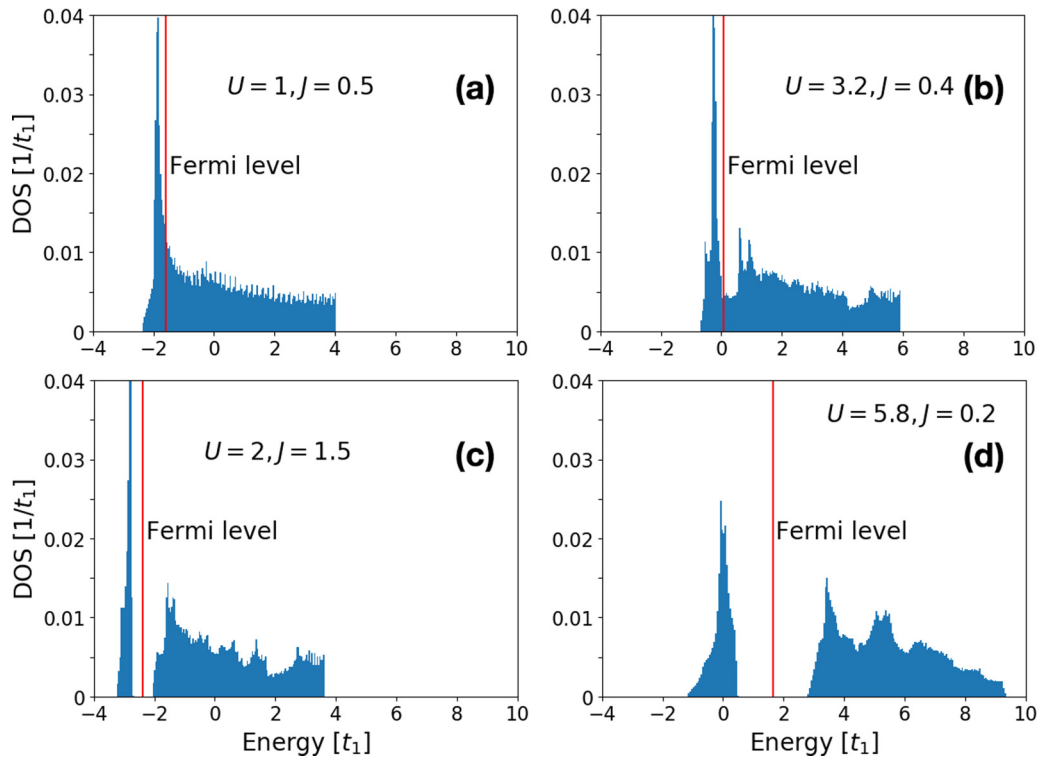


FIG. 2. Representative density of states for the various phases at  $U$  and  $J$  values marked with diamonds in Fig. 1: (a) nonmagnetic metallic phase,  $U = 1.077, J = 0.538$ ; (b) itinerant magnetic phase of type  $\uparrow\uparrow\downarrow\downarrow$ ,  $U = 3.231, J = 0.385$ ; (c) charge disproportionated, insulating phase ( $\delta \neq 0$ ), of magnetic type  $\uparrow\uparrow 0 \downarrow\downarrow 0$ , with a clear gap at the Fermi level,  $U = 2.0, J = 1.538$ ; (d) antiferromagnetic ferro-orbital (“afm-ferroorb”) Mott insulating phase,  $U = 5.846, J = 0.231$ . Other parameters as in Fig. 1. Notice the van Hove singularity at the lower band edge in all the diagrams; its presence is due to the nonzero  $t_2$  parameter, which introduces a strong asymmetry to the DOS.

in the  $U$ - $J$  plane for  $t_1 = 1, t_2 = 0.15, t_4 = 0, \epsilon_b = 0$ . We set  $t_1 = 1$  throughout this paper, so all energy scales are reported in units of  $t_1$ . Our results are in qualitative agreement with earlier findings at similar parameter values [22]. Unsurprisingly, for small values of  $U$  and  $J$ , we find  $\delta = 0$  and the system is metallic and nonmagnetic, with no gaps in its band structure, as can be seen from the typical density of states (DOS) shown in Fig. 2(a). Note that the vertical scale in the DOS plots is normed to the total volume of the crystal, i.e.,  $1/N^3$ . For large  $J$  and small-to-intermediate  $U$ , because of Hund’s rule the electrons find it preferable to occupy both orbitals at the same site, leading to ever-increasing charge modulation between neighboring sites and strong insulating behavior (and magnetic order of type  $\uparrow\uparrow 0 \downarrow\downarrow 0$ ), as can be seen from the DOS in Fig. 2(c) (this corresponds to the picture discussed in Ref. [10]). In the other extreme, for large Hubbard  $U$  and small  $J$ , no charge modulation arises because of the prohibitive cost of double occupancy. As a result, the system remains itinerant [see the DOS in Fig. 2(b)] up to fairly large values of  $U$  while acquiring magnetic character  $\uparrow\uparrow\downarrow\downarrow$ , where it switches to a spin-and-orbitally ordered Mott insulator [as can be seen from the large gap in the DOS in Fig. 2(d)]. An interesting feature in all the DOS in Fig. 2 is the van Hove singularity at the lower band edge; this is a direct consequence of the second-nearest-neighbor hopping term  $t_2 \neq 0$  and will be discussed in detail towards the end of this section.

Of course, the interesting question is how charge modulation is modified by the coupling to the lattice. To probe

this, we fix various ratios of  $J/U = 0.2, 0.3, 0.4, 0.5$  (they can be thought of as line slices of the phase diagram in Fig. 1 emanating from the origin) and tune the lattice coupling constant  $\epsilon_b$  while keeping fixed the values of the other parameters  $t_1 = 1, t_2 = 0.15, t_4 = 0.25, \alpha = 1$ . (We added the fourth-nearest-neighbor hopping to watch the lattice interact with all the ingredients of the model—explicit results on its influence on the phase diagram will be discussed below.) These results are shown in Fig. 3, while in Fig. 4 we indicate whether the HF ground state is metallic (blue) or insulating (yellow).

Clearly, for small values of  $U$  the system is metallic and homogeneous, with  $\delta = u = 0$ . Even in the absence of coupling to the lattice, i.e., when  $\epsilon_b = 0$ , with increasing  $J$  there is a transition to a state with a finite charge modulation  $\delta$ , which eventually becomes insulating if  $J$  is large enough. This MIT occurs faster for larger  $J/U$  ratios, as the tendency for two-orbital occupancy encouraged by  $J$  grows faster than the drive toward single-site occupancy coming from increased  $U$ . If the coupling to the lattice is turned on, we find that  $\delta$  increases with  $\epsilon_b$  everywhere, and the system is more likely to become insulating; thus there is positive cooperation between  $J$  and the lattice coupling  $\epsilon_b$ .

These results confirm the existence of the MIT, where the insulating state has a charge modulation  $\delta \neq 0$  and a lattice distortion  $u \neq 0$ . Coupling to the lattice increases the likelihood of this insulating ground state with finite  $u$ , as expected.

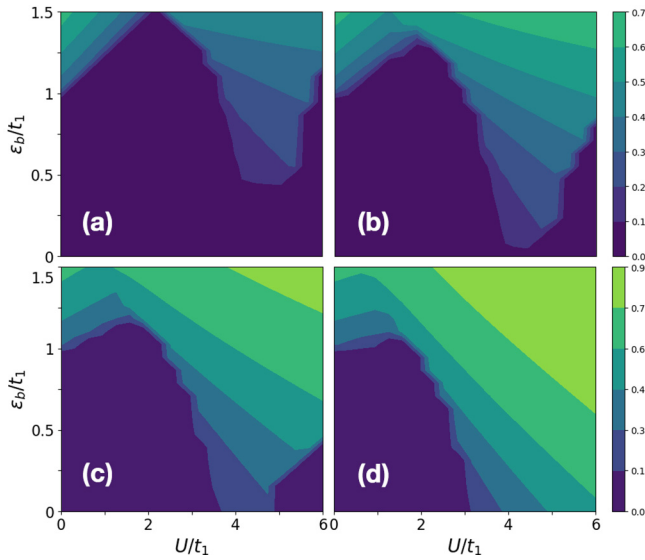


FIG. 3. Charge modulation  $\delta$  (see color scale) in the HF ground state, as a function of  $U$  and  $\epsilon_b$ , for  $J/U = 0.2, 0.3$  [(a) and (b), respectively] and  $0.4, 0.5$  [(c) and (d), respectively]. Other parameters are  $t_1 = 1, t_2 = 0.15, t_4 = 0.25, \alpha = 1$ . Resolution is  $20 \times 20$ .

We now discuss the magnetic order found in the HF ground state, and how it is influenced by the coupling to the lattice. Once again, it is useful to start with the  $U$ - $J$  plane picture. In Fig. 5 we show the magnetic order found in the HF ground state for various values of  $U$  and  $J$  both in the absence and in the presence of coupling to the lattice ( $\epsilon_b = 0$  and  $\epsilon_b = 0.8$ , respectively). The other parameters are kept fixed. The red contours indicate the corresponding value of  $\delta$ . If we fix  $\delta$  at experimentally relevant values  $\delta \approx 0.3$ – $0.4$ , we see that

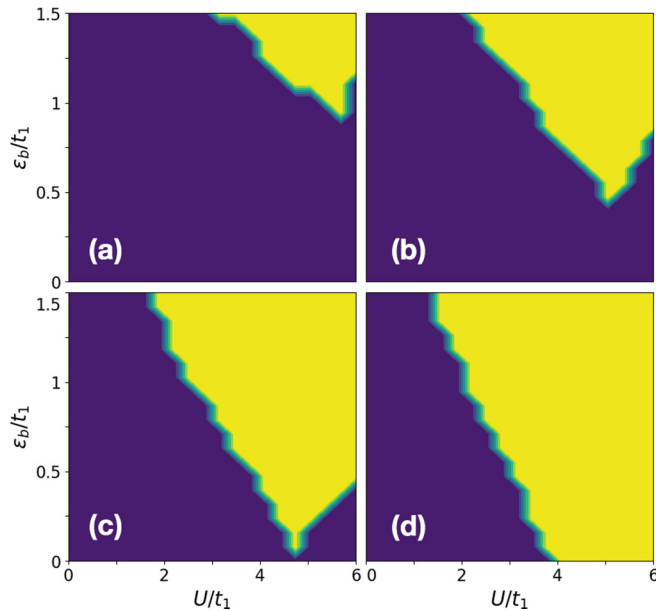


FIG. 4. The HF ground state is metallic (deep blue) or insulating (yellow). The results are shown in the  $U$ - $\epsilon_b$  space for  $J/U = 0.2, 0.3, 0.4$ , and  $0.5$ , respectively (panels arranged as in Fig. 3). All other parameters are as in Fig. 3. Resolution is  $20 \times 20$ .

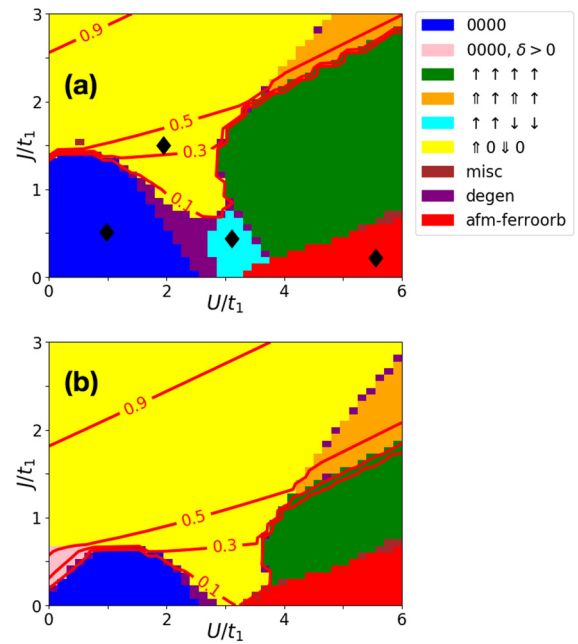


FIG. 5. (a)  $U$ - $J$  phase diagram of magnetic order, in the absence of coupling to the lattice ( $\epsilon_b = 0$ ). (b) Same when coupling to the lattice is turned on ( $\epsilon_b = 0.8$ ). Other parameters are  $t_1 = 1, t_2 = 0.15, t_4 = 0, \alpha = 1$  for both. The red-line contours indicate the value of  $\delta$ . Resolution is  $40 \times 40$ . The black diamonds mark the locations at which the densities of states are plotted in Fig. 2.

as a function of increasing  $U$  (and  $J$  adjusting accordingly) the system evolves through a variety of states. While charge modulation of the experimentally appropriate magnitude appears to originate just past the boundary of the metallic and insulating regimes at low  $U$  and intermediate  $J$ , as we follow the contour line it quickly enters the bulk of the  $\uparrow \uparrow \downarrow \downarrow$  magnetic phase already at  $U \approx 1$  before again falling on a phase line (this time between the ferromagnetic and aligned-ferrimagnetic phases) around  $U \approx 4$  for what seems like the rest of the contour. The fact that the state  $\uparrow \uparrow \downarrow \downarrow$  is favored by larger  $J$  and lies, for the most part, above these  $\delta$  values speaks in its favor as the preferred magnetic ground state. In addition, for a decently sized range of  $U$  and  $J$  values ( $U$  from 1 to 3 and  $J$  from 1 to 1.5—a range potentially consistent with experimental values for these parameters) the contour remains squarely in the  $\uparrow \uparrow \downarrow \downarrow$  phase, thus suggesting that this might be the most energetically favorable four-site spin alignment. Our phase diagram agrees qualitatively with that of Ref. [22], although there are sizable quantitative differences, which we attribute to the different form of the on-site electronic Hamiltonian used.

We note that in between the magnetic phases there are often small regions where the energies of several different magnetic orders are indistinguishable within our computational accuracy; such regions are designated “degenerate.” We emphasize that these regions do not correspond to partially disproportionated states of type  $\uparrow \uparrow \downarrow \downarrow$  (in fact, such states are never convergent within our model, see below). Instead, the states from neighboring phases (e.g.,  $\uparrow \uparrow \downarrow \downarrow$ ,  $\uparrow \uparrow \downarrow \downarrow$ , and  $\uparrow \rightarrow \downarrow \leftarrow$  in the lower middle of the phase diagram) all have the same energy per site to within  $\Delta E \sim 10^{-3}$ .

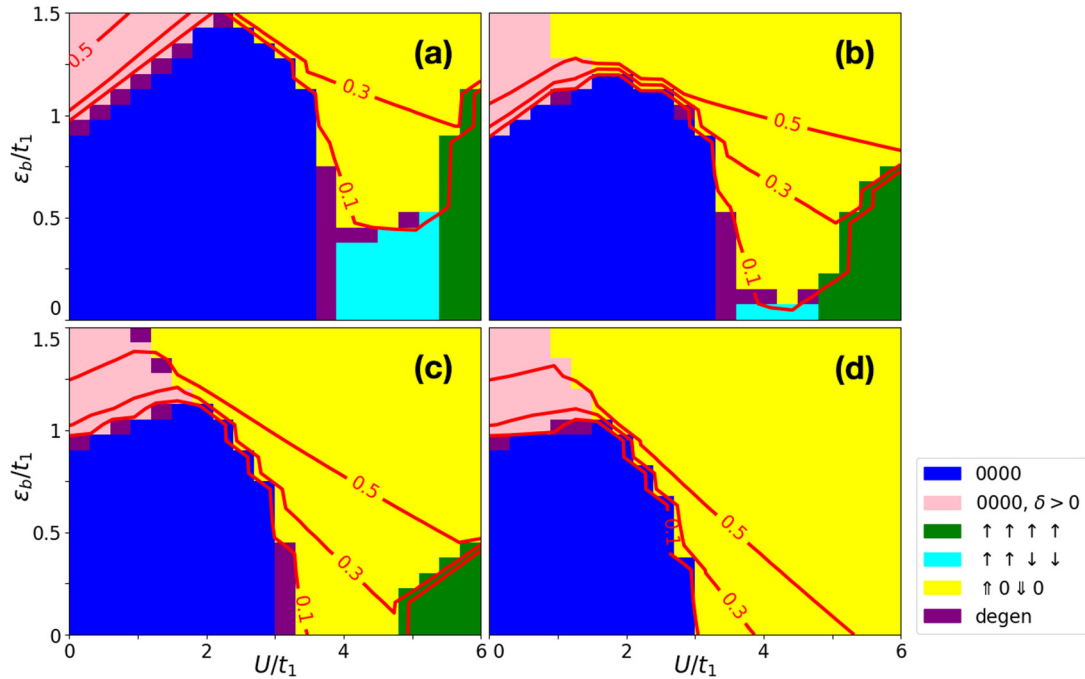


FIG. 6. Magnetic order in the HF ground state, as a function of  $U$  and  $\epsilon_b$ , for  $J/U = 0.2, 0.3$  [(a) and (b), respectively] and  $0.4, 0.5$  [(c) and (d), respectively]. Other parameters are  $t_1 = 1$ ,  $t_2 = 0.15$ ,  $t_4 = 0.25$ ,  $\alpha = 1$ .

When the coupling to the lattice is turned on, it acts to strongly reduce the energy of the charge-modulated states, as one would expect. Not only does it lead to a significant shift of the  $\uparrow 0 \downarrow 0$  magnetic order boundary, further increasing its likelihood to be the magnetic ground state, but it also shifts the charge modulation contours, leading to an enhancement of the aligned ferrimagnetic phase for large  $U$  and  $J$ , as well as the decoupling of the charge and magnetic order phase lines below  $U = 1$ , revealing a sizable metallic phase with partial charge modulation. A similar phase was noted before and interpreted as a bipolaron insulating phase in studies of the two-dimensional (2D) single-orbital Hubbard-Holstein model [38]. In that work, this phase arose only at quarter filling and for intermediate-to-large electron-lattice coupling, while at small coupling their ground state is that of free electrons, consistent with our findings. An intermediate phase also emerged in their study, where rocksaltlike charge order coincided with a  $G$ -type antiferromagnetic phase. We cannot find the analog of this 2D phase in our three-dimensional model, because it cannot be generated by any choice of a linearly coordinated unit cell that we are using.

Given this large-scale picture of the magnetic order, we once again fix ratios  $J/U$  and consider, in more detail, the impact of the lattice. The data, shown in Fig. 6, demonstrates clearly that an increase in coupling to the lattice leads to an expansion of the  $\uparrow 0 \downarrow 0$  phase boundary—the stronger the coupling to the lattice, the smaller the values of  $U$  and  $J$  that are required to stabilize the fully charged modulated magnetic order. An interesting feature of this data, already noted above, emerges in the upper-left corner of the diagrams. While typically the contours signaling the onset of charge modulation strongly follow the magnetic ordering phase lines, we see that with increased coupling to the lattice there is

a decoupling of the onset of charge and magnetic order. In other words, we obtain a charge-modulated phase without any magnetism. The lattice distortion acts to strongly gap out and flatten the band structure; however, the Fermi level is still well within the occupied band (a feature of the two-band Hubbard model), so the system stays metallic and magnetic order does not arise. Thus the coupling to the lattice acts to stabilize the charge order in the absence of magnetism and localization. This is strongly reminiscent of the decoupling of the MIT and the magnetic order transition for the Sm to Y members of the nickelate series, a well-known feature of the nickelates phase diagram, and suggests that the strength of the lattice coupling may be responsible for determining whether the charge order and the magnetic transition are concurrent or not.

We emphasize that we usually find that many of the possible four-site unit-cell magnetic orders turn out to be self-consistent within HF at the same values of parameters and that their HF energies can lie fairly close together. An example is shown in Fig. 7, where the energy corresponding to various self-consistent HF states is plotted vs  $\epsilon_b$  at fixed values of the other parameters. This is, in essence, a slice along the  $U \approx 4$  line of the top left panel in Fig. 6.

At  $\epsilon_b = 0$ , we find that the states  $\uparrow \rightarrow \downarrow \leftarrow$ ,  $\uparrow \uparrow \uparrow \uparrow$ ,  $\uparrow \uparrow \downarrow \downarrow$ , and  $\uparrow 0 \downarrow 0$  are all converged, with their HF energies per site being within  $\sim 0.001t_1$  of each other. The  $\uparrow \uparrow \downarrow \downarrow$  order has the lowest energy and thus is identified as the HF ground state. The close spacing between these energies suggests that changing any of the parameters and/or adding new ingredients—in particular, coupling to the lattice—may favor another magnetic order as the ground state. Indeed, we see that as  $\epsilon_b$  increases, the energy of the  $\uparrow 0 \downarrow 0$  state decreases and it eventually becomes the new HF ground state. Note also that the energies of the other magnetic states are independent

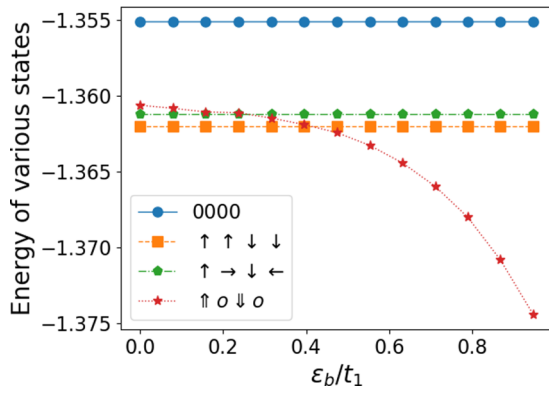


FIG. 7. Total energies of several converged self-consistent HF states as a function of  $\epsilon_b$ . The different colors correspond to different magnetic orders. The parameters are  $U = 4.105$ ,  $J = 0.2U$ ,  $t_1 = 1$ ,  $t_2 = 0.15$ ,  $t_4 = 0.25$ ,  $\alpha = 1$ .

of  $\epsilon_b$  (this pattern holds in the entire parameter space). There is a straightforward explanation to this: any state without charge modulation also has no lattice distortion, as  $\delta \sim u$  through the lattice self-consistency equation [Eq. (12)]. The real question is, Why are the states with partial charge modulation, e.g.,  $\uparrow\uparrow\downarrow\downarrow$ , not convergent within this mean-field model? Such states could potentially compete with  $\uparrow\uparrow\downarrow\downarrow$  order for ground-state status, as the coupling to the lattice is adjusted. We find that such states fail to converge no matter the starting point, and in fact they are among the least stable, as can be seen most clearly from cuts in the 15-dimensional parameter space that show iterative trajectories of the Hartree-Fock calculation (such diagrams are called “Poincaré sections” in the dynamical systems literature). In Fig. 8 we plot the evolution of the difference  $S_{1z} - S_{2z}$  versus the charge disproportionation  $\delta$ . Note that the states  $\uparrow\uparrow\downarrow\downarrow$  (central point) and  $\uparrow\uparrow\downarrow\downarrow$  (diagonal end points) are well defined in this plane. Any solution not precisely on the  $S_{1z} - S_{2z} = 0$  line converges to  $\uparrow\uparrow\downarrow\downarrow$  instead.

Next we discuss the role of the hopping amplitudes  $t_2$  and  $t_4$ . Given the spatial extent of the orbitals in the nickelates, it is unrealistic to expect them to be larger than  $t_1$ . Values

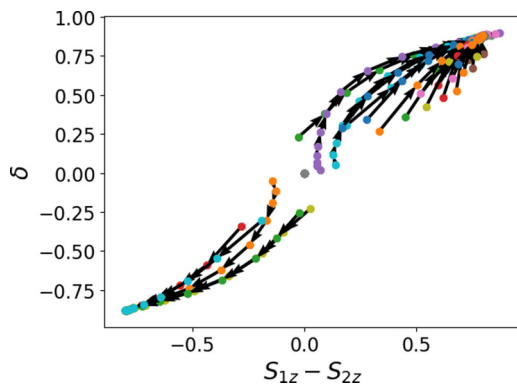


FIG. 8. A phase portrait of the iterative sequences for various starting configurations in the  $\delta$ ,  $S_{1z}$ ,  $S_{2z}$  parameter subspace. On the  $x$  axis we show  $S_{1z} - S_{2z}$ , and on the  $y$  axis we show  $\delta$ . The parameters are  $U = 5$ ,  $J = 3$ ,  $t_1 = 1$ ,  $t_2 = 0.15$ ,  $t_4 = 0.55$ ,  $\epsilon_b = 0$ .

bounded at  $t_2, t_4 < 0.3$  renormalize the overall bandwidth in the noninteracting regime by at most only 10%, which should not be enough to shift phase boundaries in the  $U$ - $J$  to any appreciable degree. And yet even small adjustments to  $t_2$  and  $t_4$  can significantly alter the magnetic phase diagram, as can be seen, for instance, in Fig. 9 for changing  $t_2$  and in Fig. 10 for changing  $t_4$ . We believe these changes to be a consequence of the shape of the DOS, which can change dramatically even for small perturbations of the hopping parameters [39]. The way a new hopping path affects the DOS can be predicted semianalytically and depends, in a hypercubic bipartite lattice, on whether the new hopping connects A-A and B-B sublattice sites, or the A-B sublattices [40].

In our case,  $t_1$  and  $t_4$  hopping produces a symmetrical (about band center) DOS, while  $t_2$  leads to a strong asymmetry and the appearance of a van Hove singularity at the lower band edge. In the spirit of the Stoner criterion, an enhancement of the density of states near the Fermi level—an effective consequence of the introduction of a nonzero  $t_2$ —lowers the value of  $U$  required for ferromagnetism to arise, thus causing the metallic region near the origin to shrink significantly (Fig. 9). Meanwhile, introducing a nonzero  $t_4$  in the presence of  $t_2$  counteracts this tendency by boosting the density of states above the Fermi level, thus increasing the interaction strength  $U$  required to exhibit magnetic order in the ground state (see Fig. 10).

On the other hand, the effect of  $t_2$  and  $t_4$  on the magnetic order competition between the various four-site contenders appears to be negligible. Figure 11 shows a typical form of the energy modulation with  $t_2$  and  $t_4$  for the chief contenders  $\uparrow\uparrow\downarrow\downarrow$ ,  $\uparrow\rightarrow\downarrow\leftarrow$ , and  $\uparrow\uparrow\downarrow\downarrow$ . The energies of the four-site states are affected in a very similar way, with none of them being the clear favorite for the ground state. In the case of  $t_4$ , the explanation for this is that the frustration costs introduced by the fourth-neighbor hopping, which connects sites that are two lattice constants apart, are identical for all of these magnetic states, so they are all equally disfavored. The effect for  $t_2$  is slightly different, as increasing it actually reduces the energy of all of the magnetic states, initially showing a slight preference for the noncollinear  $\uparrow\rightarrow\downarrow\leftarrow$ , then the collinear  $\uparrow\uparrow\downarrow\downarrow$ , and finally the FM state. This can be understood in the spirit of the Stoner effect, which is somewhat more general in this two-band Hubbard model: as the density of states at the Fermi level grows, most kinds of magnetic order benefit, but the FM state benefits the most. The strong response of the FM state to the hopping amplitude modulations can be readily seen in both Figs. 11(a) and 11(b). The state suffers most strongly due to the added frustrations from  $t_4$  and benefits the most from the Stoner effect with  $t_2$ . Notice that all of these effects occur with minimal bandwidth renormalization, as discussed; instead, they are consequences of the shape of the DOS.

Finally, we comment on the role played by the  $\alpha$  anharmonicity parameter. Given the form of the lattice energy  $E_{\text{latt}} = \epsilon_b(u_i^2 + \alpha u_i^4/2)$  and a typical value for lattice distortion  $u_i \approx 0.5$ , we see that the two terms compare numerically as  $\epsilon_b(0.25 + 0.03\alpha)$ . Thus for  $\alpha = 1$  the quartic correction is merely 10% of the quadratic contribution and serves only to modulate the bare magnitude of the lattice distortion  $u$ , as determined by Eq. (12), away from  $u = \delta$ , without affecting

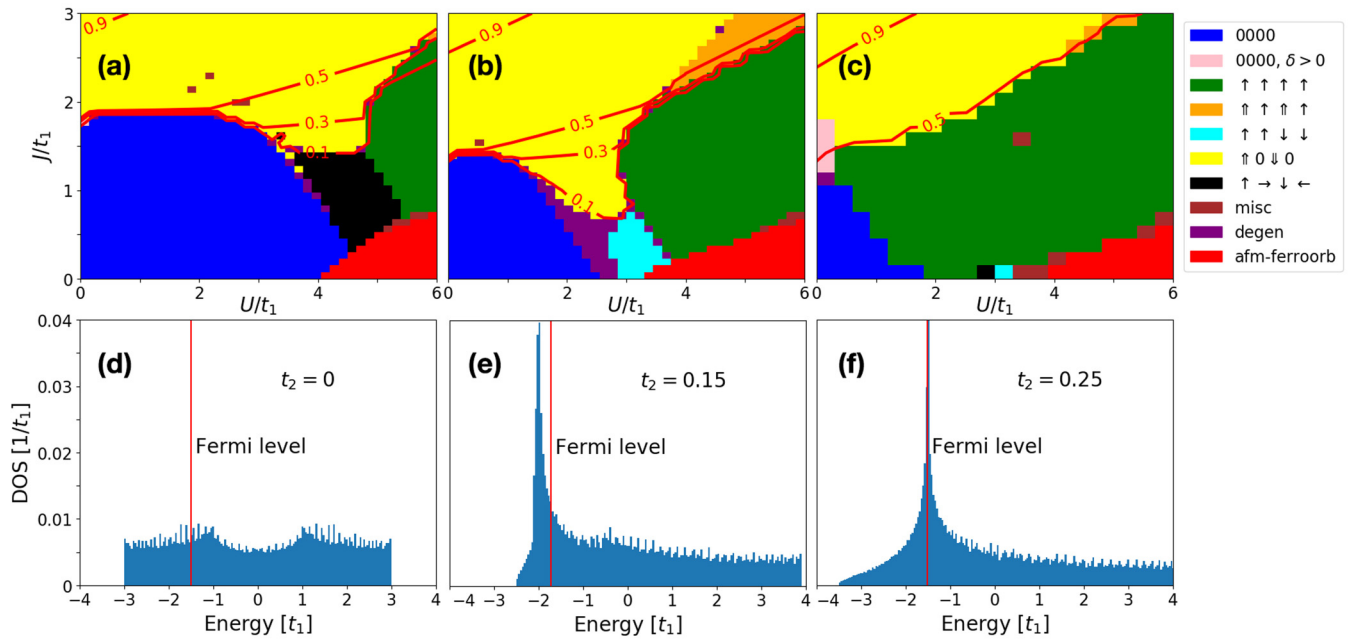


FIG. 9. Magnetic order in the HF ground state, as a function of  $U$  and  $J$ , for  $t_2 = 0, 0.15, 0.25$  [(a), (b), and (c), respectively]. Other parameters are  $t_1 = 1, t_4 = 0, \epsilon_b = 0$ . In (d), (e), and (f) we depict the noninteracting ( $U = J = 0$ ) DOS that correspond to the systems (a), (b), and (c), respectively. Notice that increasing the bandwidth (even if just modestly by at most 15%), paradoxically, leads to more robust ferromagnetism at *lower*  $U$ —a consequence of the van Hove singularity at the lower band edge. Also notice how when the next-nearest-neighbor frustration is maximally reduced ( $t_2 = 0$ ), the noncollinear four-site magnetic order dominates the collinear one. Currently it is not clear to us why this would be the case, given how introducing  $t_2, t_4$  seems to affect them equally based on pure lattice frustration arguments.

the basic physics of the problem. The results shown in Fig. 12 confirm as much. Insofar as the charge modulation contours are displaced from their position at  $\alpha = 0$ , it is the ones closest

to  $\delta = 1$  and thus with the largest  $u$  that are affected the most, while the rest of the phase diagram remains the same. In the interest of controlling the size of the lattice distortion, all the

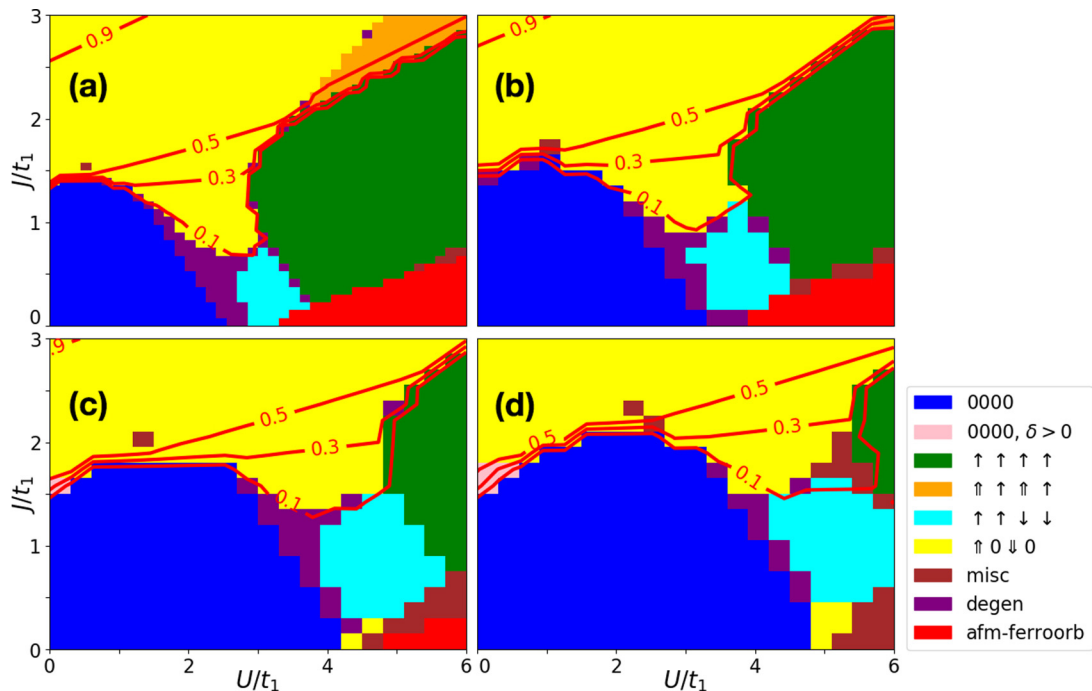


FIG. 10. Magnetic order in the HF ground state as a function of  $U$  and  $J$  for  $t_4 = 0, 0.1$  [(a) and (b), respectively] and  $t_4 = 0.25, 0.35$  [(c) and (d), respectively]. The bandwidth is  $W = 6.4$  in all cases. Other parameters are  $t_1 = 1, t_2 = 0.15, \epsilon_b = 0$ . The growth of the metallic region is clearly not the effect of a renormalized bandwidth but rather is due to the changes of the shape of the DOS.

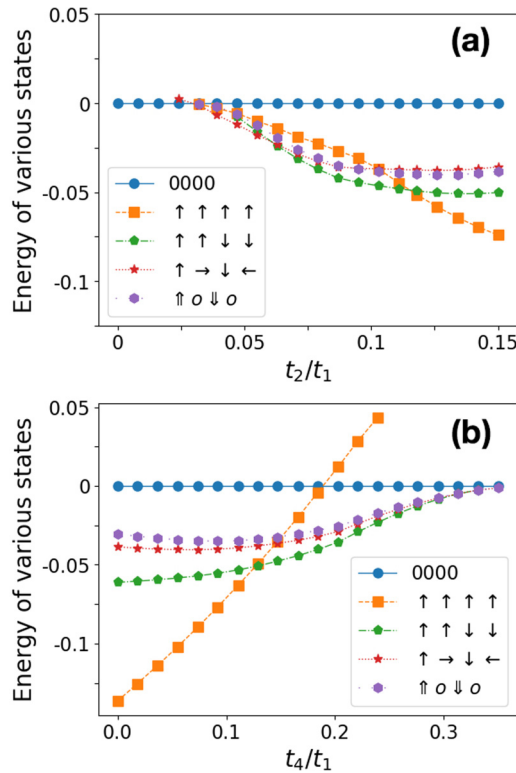


FIG. 11. Energies of several converged self-consistent HF states as a function of  $t_2$  (a) and  $t_4$  (b), respectively, relative to the energy of the metallic state. The different colors correspond to different magnetic orders (see the legend). The parameters are  $U = 4, J = 0.316, t_1 = 1, t_4 = 0, \epsilon_b = 0$  for (a) and  $U = 5, J = 0.316, t_1 = 1, t_2 = 0.15, \epsilon_b = 0$  for (b). Notice how in (b) the relative energies of the chief magnetic ground-state contenders are not affected much by the change—except for ferromagnetism, which gets strongly frustrated with the additional  $t_4$  hopping and, paradoxically, “unfrustrated” with the introduction of  $t_2$  hopping due to DOS effects (see the text for details). Meanwhile, in (a) with tuning the  $t_2$  rate away from 0 the noncollinear  $\uparrow \rightarrow \downarrow \leftarrow$  gets briefly favored, but then quickly loses out to the collinear  $\uparrow \uparrow \downarrow \downarrow$ , before ferromagnetism sets in.

calculations in this paper were carried out at  $\alpha = 1$ , unless indicated otherwise.

## V. CONCLUSIONS

The magnetic order of the rare-earth nickelate series, much like the metal-insulator behavior and charge order, can be expected to couple to the lattice degrees of freedom. Even the simplest semiclassical version of the Holstein coupling is sufficient to aid charge disproportionation and to turn the material into an insulator in much of the parameter space. While several magnetic orders converge to self-consistency in our effective two-band Hubbard model for the nickelates, the  $\uparrow \uparrow \downarrow \downarrow$  antiferromagnetic order dominates, usually presenting together with charge disproportionation  $\delta \neq 0$ . In contrast, the nondisproportionated collinear  $\uparrow \uparrow \downarrow \downarrow$  and noncollinear  $\uparrow \rightarrow \downarrow \leftarrow$  orders only arise at intermediate/large  $U$  and small  $J$  and do not fare well when the coupling to the lattice

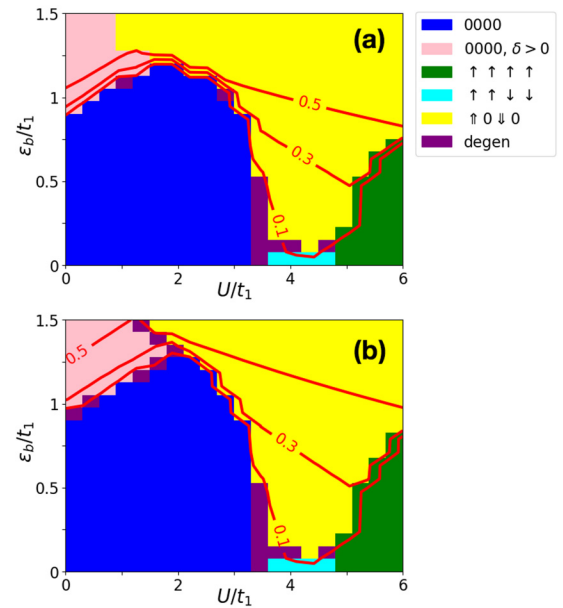


FIG. 12. Magnetic order in the HF ground state as a function of  $U$  and  $\epsilon_b$  for  $J/U = 0.2$  and two different values of the anharmonicity  $\alpha$ : (a)  $\alpha = 0$  and (b)  $\alpha = 1$ . Other parameters are  $t_1 = 1, t_2 = 0.15, t_4 = 0.25$ .

is increased, instead quickly disappearing from the phase diagram entirely. This can be easily understood, as the nondisproportionated modes cannot couple to the lattice distortion, given that for them  $\delta = 0$  and hence, via the self-consistency condition, also  $u = 0$ . Thus the main impact of the lattice on the magnetic order, in our model and at the HF level, is to make the  $\uparrow \uparrow \downarrow \downarrow$  order even more dominant by decreasing its energy relative to that of the other states. Surprisingly, we find that self-consistency is never achieved for a state such as  $\uparrow \rightarrow \downarrow \leftarrow$  or  $\uparrow \uparrow \downarrow \downarrow$ , that is, for  $\delta \neq 0$  [9,23]. Such states are unstable in the iterative sequences, with the slightest deviations from their expected mean-field parameter structure leading to fast flow towards the stable solution  $\uparrow \uparrow \downarrow \downarrow$ .

While usually the charge-modulated phase  $\delta \neq 0$  always occurs with  $\uparrow \uparrow \downarrow \downarrow$  for small  $U$ , we found that introducing a finite electron-lattice coupling  $\epsilon_b$  also stabilizes a new phase, where the charge modulation persisted on its own, without any associated magnetic order. The magnetic order would then arise only at higher  $J$ , leading to the effective decoupling of the charge modulation and magnetic transitions—a feature strongly reminiscent of the canonical nickelates phase diagram.

We therefore conclude that all else being equal, coupling to the lattice favors the  $\uparrow \uparrow \downarrow \downarrow$  order. However, one must keep in mind that our simplified Hamiltonian may fail to capture properly some aspects of the actual physics of these materials, especially in the NCT scenario where the O sites should be included explicitly. Moreover, it is known that the accuracy of the Hartree-Fock approximation can become questionable as the strongly correlated limit is approached. One caveat to note is that because of the negative charge transfer, significant overlap between the (wide) O  $2p$  bands and the Ni  $3d$  bands should reduce the effective  $U$  value (thus

reducing the strength of correlations), explaining why many in the literature have had success using a Hartree-Fock approach on the nickelate problem [17,19,21,27]. In addition to the question of the validity of the mean-field approach, other open questions remain. Specifically, the nature of the orbitally and magnetically ordered state we found at intermediate to large  $U$  (i.e., close to the Mott regime), and other orbital orders possible within the model, are not entirely clear and their investigation is left to future studies. Overall, strong  $t_{pd}$  covalency places nickelates in the intermediate coupling regime of  $U/W$  (for instance, see Ref. [41]), wherein charge fluctuations coupled to lattice become an increasingly important factor in the magnetic phase behavior of these materials. While the present study treating the lattice semiclassically is a reasonable starting point, the pronounced polaron effects observed in nickelates [42] suggest that a quantum-dynamical treatment of the electron-lattice coupling problem should be the next essential step towards understanding the physics of these materials.

### ACKNOWLEDGMENTS

The authors are grateful to George Sawatzky for valuable discussions about the model and the material series. We would also like to acknowledge the invaluable help of Ev-

genia Krichanovskaya with the graphic design of the various plots and diagrams. This work was supported by the UBC Stewart Blusson Quantum Matter Institute, the Max-Planck-UBC-UTokyo Center for Quantum Materials, and the Natural Sciences and Engineering Research Council of Canada.

### APPENDIX A: HOPPING OPERATOR

The hopping operator is a sum of three terms

$$\hat{T} = \hat{T}_1 + \hat{T}_2 + \hat{T}_4, \quad (\text{A1})$$

where

$$\hat{T}_1 = -t_1 \sum_{i\sigma} \sum_{\eta=x,y,z} (d_{i\eta\sigma}^\dagger d_{i+\eta,\eta\sigma} + \text{H.c.}), \quad (\text{A2})$$

$$\hat{T}_2 = -t_2 \sum_{\substack{i\eta\mu\sigma, \\ \eta \neq \mu \\ \eta, \mu = x, y, z}} (d_{i+\mu+\eta,\mu\sigma}^\dagger d_{i\eta\sigma} + \text{H.c.}), \quad (\text{A3})$$

$$\hat{T}_4 = -t_4 \sum_{i\sigma} \sum_{\eta=x,y,z} (d_{i\eta\sigma}^\dagger d_{i+2\eta,\eta\sigma} + \text{H.c.}). \quad (\text{A4})$$

After a Fourier transform and factorization, the hopping operator has the form

$$\hat{T} = \sum_{\mathbf{k}\sigma} [t_{zz}(\mathbf{k}) d_{\mathbf{k}z\sigma}^\dagger d_{\mathbf{k}z\sigma} + t_{\bar{z}\bar{z}}(\mathbf{k}) d_{\mathbf{k}\bar{z}\sigma}^\dagger d_{\mathbf{k}\bar{z}\sigma} + t_{z\bar{z}}(\mathbf{k}) (d_{\mathbf{k}z\sigma}^\dagger d_{\mathbf{k}\bar{z}\sigma} + d_{\mathbf{k}\bar{z}\sigma}^\dagger d_{\mathbf{k}z\sigma})], \quad (\text{A5})$$

with the definitions

$$\begin{aligned} t_{zz}(\mathbf{k}) &= -2t_1 \left( \cos(k_z) + \frac{1}{4} [\cos(k_x) + \cos(k_y)] \right) - 2t_4 \left( \cos(2k_z) + \frac{1}{4} [\cos(2k_x) + \cos(2k_y)] \right) \\ &\quad - 2t_2 \{ \cos(k_x) \cos(k_y) - 2 \cos(k_z) [\cos(k_y) + \cos(k_x)] \}, \\ t_{\bar{z}\bar{z}}(\mathbf{k}) &= -\frac{3t_1}{2} [\cos(k_x) + \cos(k_y)] - \frac{3t_4}{2} [\cos(2k_x) + \cos(2k_y)] + 6t_2 \cos(k_x) \cos(k_y), \\ t_{z\bar{z}}(\mathbf{k}) &= \frac{\sqrt{3}t_1}{2} [\cos(k_x) - \cos(k_y)] + \frac{\sqrt{3}t_4}{2} [\cos(2k_x) - \cos(2k_y)] - 2\sqrt{3}t_2 \cos(k_z) [\cos(k_x) - \cos(k_y)]. \end{aligned}$$

### APPENDIX B: MINIMIZING LATTICE CONTRIBUTIONS

In the text we were faced with the need to solve the cubic equation

$$u^3 + \frac{1}{\alpha}u - \frac{\delta}{\alpha} = 0, \quad (\text{B1})$$

which arose during lattice energy minimization in the Hartree-Fock process. As we mentioned, it admits a closed-form solution using Cardano's formula. More explicitly, write

$$u^3 = (s - t)^3, \quad \frac{1}{\alpha} = 3st, \quad \frac{\delta}{\alpha} = s^3 - t^3.$$

Combining the latter two equations into one for  $t$ , we find

$$t^6 + t^3 \left( \frac{\delta}{\alpha} \right) - \left( \frac{1}{3\alpha} \right)^3 = 0,$$

which is easily solved as a quadratic,

$$t^3 = \frac{1}{2} \left( -\frac{\delta}{\alpha} \pm \sqrt{\left( \frac{\delta}{\alpha} \right)^2 + \frac{4}{27\alpha^3}} \right),$$

$$s^3 = t^3 + \frac{\delta}{\alpha} = \frac{1}{2} \left( \frac{\delta}{\alpha} \pm \sqrt{\left( \frac{\delta}{\alpha} \right)^2 + \frac{4}{27\alpha^3}} \right),$$

from which we can recover the expression for  $u$  in Eq. (12).

## APPENDIX C: FULL MEAN-FIELD HAMILTONIAN

The full effective Hamiltonian is

$$\begin{aligned}
\hat{H}_{\text{HF}} = & \sum_{\mathbf{k}ab\sigma} t_{ab}(\mathbf{k}) d_{\mathbf{k}a\sigma}^\dagger d_{\mathbf{k}b\sigma} + \sum_{\mathbf{k}a\sigma} \left( \frac{3U - 5J}{4} - \frac{\sigma}{2}(U + J)S_{\text{FM}} \right) d_{\mathbf{k}a\sigma}^\dagger d_{\mathbf{k}a\sigma} \\
& + \left( \frac{3U - 5J}{4} \delta - 2\epsilon_b u - \frac{\sigma}{2}(U + J)S_{\text{AFM}} \right) d_{\mathbf{k}+\mathbf{Q}_{c,a\sigma}}^\dagger d_{\mathbf{k}a\sigma} \\
& - \frac{\sigma}{4}(U + J)((S_{1z} - iS_{2z})d_{\mathbf{k}+\mathbf{Q}_m,a\sigma}^\dagger d_{\mathbf{k}a\sigma} + (S_{1z} + iS_{2z})d_{\mathbf{k}-\mathbf{Q}_m,a\sigma}^\dagger d_{\mathbf{k}a\sigma}) \\
& - \frac{U + J}{4}((S_{1x} - iS_{2x})d_{\mathbf{k}+\mathbf{Q}_m,a\sigma}^\dagger d_{\mathbf{k}a\bar{\sigma}} + (S_{1x} + iS_{2x})d_{\mathbf{k}-\mathbf{Q}_m,a\sigma}^\dagger d_{\mathbf{k}a\bar{\sigma}}) \\
& - \frac{U - J}{2}((X_1 - iX_2)d_{\mathbf{k}+\mathbf{Q}_m,a\sigma}^\dagger d_{\mathbf{k}a\bar{\sigma}} + (S_{1x} + iS_{2x})d_{\mathbf{k}-\mathbf{Q}_m,a\sigma}^\dagger d_{\mathbf{k}a\bar{\sigma}}) \\
& + [(5J - U)O_1 - \sigma(U - J)Z_1]d_{\mathbf{k}a\sigma}^\dagger d_{\mathbf{k}a\bar{\sigma}} + [(5J - U)O_2 - \sigma(U - J)Z_2]d_{\mathbf{k}+\mathbf{Q}_{c,a\sigma}}^\dagger d_{\mathbf{k}a\bar{\sigma}} \\
& - \frac{\sigma}{2}(U - J)[(Z_3 - iZ_4)d_{\mathbf{k}+\mathbf{Q}_m,a\sigma}^\dagger d_{\mathbf{k}a\bar{\sigma}} + (Z_3 + iZ_4)d_{\mathbf{k}-\mathbf{Q}_m,a\sigma}^\dagger d_{\mathbf{k}a\bar{\sigma}}].
\end{aligned}$$

## APPENDIX D: HARTREE-FOCK ENERGY

The full expression for the electron-electron interactions part of the Hamiltonian in a Hartree-Fock state  $|\Psi_e\rangle$  is given by

$$\begin{aligned}
\frac{1}{N}\langle \hat{H}_e \rangle = & \frac{3U - 5J}{8}(1 + \delta^2) - \frac{U + J}{2}(S_{\text{FM}}^2 + S_{\text{AFM}}^2 + \frac{S_{1x}^2 + S_{1z}^2 + S_{2x}^2 + S_{2z}^2}{2}) - 2(U - 5J)(O_1^2 + O_2^2) \\
& - 2(U - J)\left(Z_1^2 + Z_2^2 + \frac{Z_3^2 + Z_4^2}{2}\right) - (U - J)(X_1^2 + X_2^2).
\end{aligned} \tag{D1}$$

- 
- [1] G. Catalan, *Phase Transitions* **81**, 729 (2008).
- [2] M. L. Medarde, *J. Phys.: Condens. Matter* **9**, 1679 (1997).
- [3] M. Hepting, *Ordering Phenomena in Rare-Earth Nickelate Heterostructures*, Springer Theses (Springer International Publishing, Cham, 2017).
- [4] G. Giovannetti, S. Kumar, D. Khomskii, S. Picozzi, and J. van den Brink, *Phys. Rev. Lett.* **103**, 156401 (2009).
- [5] N. A. Spaldin, *MRS Bull.* **42**, 385 (2017).
- [6] J. F. Scott, *Nat. Mater.* **6**, 256 (2007).
- [7] These octahedral cages undergo a variety of tilts, twists, and other complicated distortions due to the rare-earth ion being too small to accommodate a true perovskite lattice. However, such distortions change little across the temperature range we are interested in; the main change to lattice structure comes from the breathing-mode distortion [43]. As such, for the purposes of our analysis we can focus on the breathing-mode distortion.
- [8] J. Rodríguez-Carvajal, S. Rosenkranz, M. Medarde, P. Lacorre, M. T. Fernandez-Díaz, F. Fauth, and V. Trounov, *Phys. Rev. B* **57**, 456 (1998).
- [9] V. Scagnoli, U. Staub, A. M. Mulders, M. Janousch, G. I. Meijer, G. Hammerl, J. M. Tonnerre, and N. Stojic, *Phys. Rev. B* **73**, 100409(R) (2006).
- [10] I. I. Mazin, D. I. Khomskii, R. Lengsdorf, J. A. Alonso, W. G. Marshall, R. M. Ibberson, A. Podlesnyak, M. J. Martínez-Lope, and M. M. Abd-Elmeguid, *Phys. Rev. Lett.* **98**, 176406 (2007).
- [11] M. Medarde, C. Dallera, M. Grioni, B. Delley, F. Vernay, J. Mesot, M. Sikora, J. A. Alonso, and M. J. Martínez-Lope, *Phys. Rev. B* **80**, 245105 (2009).
- [12] T. Mizokawa, D. I. Khomskii, and G. A. Sawatzky, *Phys. Rev. B* **61**, 11263 (2000).
- [13] H. Park, A. J. Millis, and C. A. Marianetti, *Phys. Rev. Lett.* **109**, 156402 (2012).
- [14] D. Puggioni, A. Filippetti, and V. Fiorentini, *Phys. Rev. B* **86**, 195132 (2012).
- [15] A. D. Caviglia, R. Scherwitzl, P. Popovich, W. Hu, H. Bromberger, R. Singla, M. Mitrano, M. C. Hoffmann, S. Kaiser, P. Zubko, S. Gariglio, J.-M. Triscone, M. Först, and A. Cavalleri, *Phys. Rev. Lett.* **108**, 136801 (2012).
- [16] B. Lau and A. J. Millis, *Phys. Rev. Lett.* **110**, 126404 (2013).
- [17] S. Johnston, A. Mukherjee, I. Elfimov, M. Berciu, and G. A. Sawatzky, *Phys. Rev. Lett.* **112**, 106404 (2014).
- [18] J. L. García-Muñoz, J. Rodríguez-Carvajal, P. Lacorre, and J. B. Torrance, *Phys. Rev. B* **46**, 4414 (1992).
- [19] J. L. García-Muñoz, J. Rodríguez-Carvajal, and P. Lacorre, *Europhys. Lett.* **20**, 241 (1992).
- [20] A. Muñoz, J. Alonso, M. Martínez-Lope, and M. Fernández-Díaz, *J. Solid State Chem.* **182**, 1982 (2009).
- [21] K. Haule and G. L. Pascut, *Sci. Rep.* **7**, 10375 (2017).
- [22] S. B. Lee, R. Chen, and L. Balents, *Phys. Rev. B* **84**, 165119 (2011).
- [23] Y. Lu, D. Betto, K. Fürsich, H. Suzuki, H.-H. Kim, G. Cristiani, G. Logvenov, N. B. Brookes, E. Benckiser, M. W. Haverkort,

- G. Khaliullin, M. Le Tacon, M. Minola, and B. Keimer, *Phys. Rev. X* **8**, 031014 (2018).
- [24] J. Kanamori, *Prog. Theor. Phys.* **30**, 275 (1963).
- [25] A. M. Oleś, *Phys. Rev. B* **28**, 327 (1983).
- [26] A. B. Georgescu and S. Ismail-Beigi, *Phys. Rev. B* **92**, 235117 (2015).
- [27] C. Castellani, C. R. Natoli, and J. Ranninger, *Phys. Rev. B* **18**, 4945 (1978).
- [28] A. Subedi, O. E. Peil, and A. Georges, *Phys. Rev. B* **91**, 075128 (2015).
- [29] H. Hellmann, in *Hans Hellmann: Einführung in die Quantenchemie* (Springer Berlin Heidelberg, Berlin, 2015), pp. 19–376.
- [30] R. P. Feynman, *Phys. Rev.* **56**, 340 (1939).
- [31] D. J. Griffiths, *Introduction to Quantum Mechanics*, 2nd ed. (Pearson Prentice Hall, Toronto, 2005), pp. 287–288.
- [32] F. Jensen, *Introduction to Computational Chemistry*, 2nd ed. (John Wiley & Sons Inc., Mississauga, 2007), pp. 321–323.
- [33] That is a cubic equation lacking a quadratic term.
- [34] T. Mizokawa and A. Fujimori, *Phys. Rev. B* **54**, 5368 (1996).
- [35] R. Peters, Magnetic Phases in the Hubbard Model, Ph.D. thesis, der Georg-August-Universität Göttingen, 2009.
- [36] A. S. Banerjee, P. Suryanarayana, and J. E. Pask, *Chem. Phys. Lett.* **647**, 31 (2016).
- [37] P. Pulay, *Chem. Phys. Lett.* **73**, 393 (1980).
- [38] S. Kumar and J. van den Brink, *Phys. Rev. B* **78**, 155123 (2008).
- [39] R. Peters and T. Pruschke, *Phys. Rev. B* **79**, 045108 (2009).
- [40] M. Eckstein, M. Kollar, K. Byczuk, and D. Vollhardt, *Phys. Rev. B* **71**, 235119 (2005).
- [41] T. Mizokawa, A. Fujimori, T. Arima, Y. Tokura, N. Mori, and J. Akimitsu, *Phys. Rev. B* **52**, 13865 (1995).
- [42] R. Jaramillo, S. D. Ha, D. M. Silevitch, and S. Ramanathan, *Nat. Phys.* **10**, 304 (2014).
- [43] Y. Bodenthin, U. Staub, C. Piamonteze, M. García-Fernández, M. J. Martínez-Lope, and J. A. Alonso, *J. Phys.: Condens. Matter* **23**, 036002 (2011).